Magnetic phase diagram of cubic perovskites $SrMn_{1-x}Fe_xO_3$

S. Kolesnik, B. Dabrowski, J. Mais, D. E. Brown, R. Feng, O. Chmaissem, R. Kruk,* and C. W. Kimball
Department of Physics, Northern Illinois University, DeKalb, Illinois 60115

(Received 9 July 2002; revised manuscript received 5 November 2002; published 2 April 2003)

We combine the results of magnetic and transport measurements with Mössbauer spectroscopy and room-temperature diffraction data to construct the magnetic phase diagram of the family of cubic perovskite manganites $SrMn_{1-x}Fe_xO_3$. We have found antiferromagnetic ordering for lightly and heavily Fe-substituted material, while intermediate substitution leads to spin-glass behavior. Near the $SrMn_{0.5}Fe_{0.5}O_3$ composition these two types of ordering are found to coexist and affect one another. The spin-glass behavior may be caused by competing ferro- and antiferromagnetic interactions among Mn^{4+} and observed Fe^{3+} and Fe^{5+} ions.

DOI: 10.1103/PhysRevB.67.144402 PACS number(s): 75.30.Kz, 75.50.Ee, 75.50.Lk, 81.30.Dz

I. INTRODUCTION

Perovskite manganites, $AMnO_3$, have been studied in great detail during the past several years because of very interesting magnetic and electronic properties resulting from competing charge, exchange, and phonon interactions.[1] Insulating *A*-, *C*-, *CE*-, and *G*-type antiferromagnetic (AFM), metallic ferromagnetic, and charge or orbital ordering properties can be tuned over a wide range through the choice of size and charge of the *A*-site cations which control the degree of structural distortions and the formal valence of Mn. Recently, increased interest has focused on the colossal magnetoresistive effect and the destruction of the charge ordering induced by substitutions on the Mn site.[2]

From the point of view of competing interactions, the stoichiometric $SrMn_{1-x}Fe_xO_3$ system is interesting because it should contain Mn^{+4} (t_{2g}^3) and Fe^{+4} ($t_{2g}^3e_g^1$) ions. The *G*-type AFM ($T_N=233$ K) and insulating $SrMnO_3$ can be obtained in a cubic perovskite form through a two-step synthesis procedure,[3] although many previous studies focused on the hexagonal phase that is stable in air at $T<1440\,^{\circ}C$. We have recently shown that the *G*-type AFM phase is preserved for single-valent Mn^{4+} in $Sr_{1-x}Ca_xMnO_3$ in the cubic, tetragonal, and orthorhombic crystal structures.[4] T_N is suppressed by the bending of the Mn-O-Mn bond angle from 180° and by the variance of the average size of the *A*-site ion via changes in the Sr/Ca ratio.[5] The other end member of the series, $SrFeO_3$, is also a cubic perovskite with a helical AFM structure ($T_N=134$ K).[6] The low resistivity ($\sim 10^{-3}\ \Omega$ cm) and metallic character when fully oxygenated[7,8] was considered the reason for the absence of the Jahn-Teller distortion and orbital ordering of Fe^{4+}. Deviations from oxygen stoichiometry in $SrFeO_{3-\delta}$ lead to a formation of several different oxygen-vacancy-ordered perovskite structures for $\delta=1/8$, 1/4, and 1/2.[9] The substitution of Co for Fe yields a $SrFe_{1-x}Co_xO_3$ compound, which is ferromagnetic for $x\geqslant 0.2$ with a large negative magnetoresistance for $0\leqslant x\leqslant 0.7$.[10] Several oxygen-deficient $SrMn_{1-x}Fe_xO_{3-\delta}$ compositions have recently been studied.[11] The orthorhombically distorted perovskite $CaFeO_3$ compound was shown to undergo the charge separation to Fe^{5+} (t_{2g}^3) and Fe^{3+} ($t_{2g}^3e_g^2$).[12] The highly energetically stable high-spin configuration was cited as a reason for this behavior. This charge disproportionation phenomenon can also be observed in $Ca_{1-x}Sr_xFeO_3$,[13] $La_{1-x}Sr_xFeO_3$,[14] and $SrMn_{1-x}Fe_xO_{3-\delta}$.[11]

In this study, we investigate polycrystalline $SrMn_{1-x}Fe_xO_3$. We have constructed the magnetic phase diagram for fully oxygenated samples. We observe an antiferromagnetic order for Fe content $x\leqslant 0.5$ and $x\geqslant 0.9$. For intermediate Fe content $0.3\leqslant x\leqslant 0.8$ we observe a spin-glass behavior with features characteristic of ''ideal'' three-dimensional Ising spin glasses. Increasing the Fe content leads to significant covalency effects, such as a decrease of resistivity and covalent shortening of the lattice parameter. We also observe Fe^{3+}/Fe^{5+} charge disproportionation in stoichiometric $SrMn_{1-x}Fe_xO_3$.

II. EXPERIMENTAL DETAILS

The samples were prepared using a two-step synthesis method developed for similar kinetically stable perovskites.[15] First, oxygen-deficient samples were prepared in argon at $T=1300-1400\,^{\circ}C$ for $x\leqslant 0.5$ and in air at $1300\,^{\circ}C$ for $x>0.5$. The samples were then annealed in air or O_2 at lower temperatures to achieve stoichiometric compositions with respect to the oxygen content. High-pressure O_2 in the range of 140–600 bars was applied for $x\geqslant 0.1$. High-pressure annealing is essential to produce fully oxygenated samples. The oxygen content in the $x=0.5$ sample was controlled within the range 2.86–3.00 by annealing the sample under partial pressure of oxygen between 10^{-4} and 600 bars on a thermobalance or in a high-pressure furnace. The samples annealed in the furnace were carefully weighed before and after annealing and the oxygen content was determined from the mass difference. The ac susceptibility, dc magnetization, and resistivity were measured using a physical property measurement system model 6000 (Quantum Design). X-ray-diffraction patterns were collected using a Rigaku diffractometer. Powder neutron diffraction was performed at the Intense Pulsed Neutron Source at Argonne National Laboratory. Both x-ray- and neutron-diffraction data were refined using general structure analysis system software. Typical diffraction patterns are presented in Fig. 1. Mössbauer measurements were performed in transmission geometry using 50-mCi ^{57m}Co in an Rh source kept at room

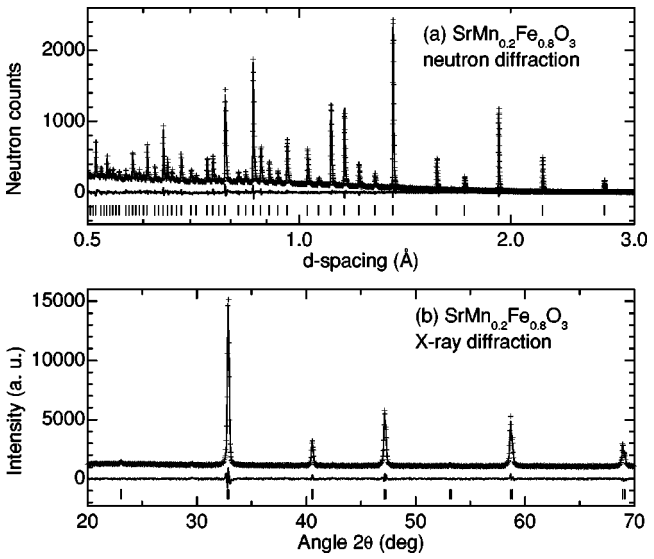

FIG. 1. Diffraction patterns for $SrMn_{0.2}Fe_{0.8}O_3$. Crosses are observed data points. The solid lines through the data are the Rietveld refinement patterns. The solid lines below the diffraction patterns represent the differences between the observed and calculated intensities. The ticks at the bottom mark the peak positions.

temperature and a krypton proportional detector. The samples measured at 5 K and 293 K were placed in an exchange gas cryostat cooled with liquid helium. Silicon diode sensors allowed the control and stabilization of temperature to within ± 0.1 K.

III. STRUCTURAL DATA

All synthesized samples were single phase with a primitive cubic $Pm\text{-}3m$ crystal structure. The structure can be simply described as a three-dimensional stacking of corner-sharing $(Mn,Fe)O_6$ regular octahedra formed by six equivalent randomly distributed Mn-O or Fe-O bonds. Figure 2 shows the a-axis lattice parameter for $SrMn_{1-x}Fe_xO_3$. We also present previously determined values of a for $SrFeO_3$ (Ref. 9) and $SrMn_{1-x}Fe_xO_{3-\delta}$ from Ref. 11. The a-axis lattice parameter systematically increases with increasing content of the larger Fe ion substituted for Mn. The slope of the a vs x dependence is smaller for larger x, which indicates the increasing role of the covalency of the Fe-O bond. By studying the structural data for samples with the oxygen content $3-\delta$ (determined from the thermogravimetric analysis), we also found that the lattice parameter, a, linearly increases with decreasing oxygen content. For example, for $x=0.5$, the rate of this increase is 0.064(2) Å per oxygen atom in the formula unit. Hence, we conclude that the difference of the lattice parameter between our results and those of Ref. 11 is a result of different oxygen contents.

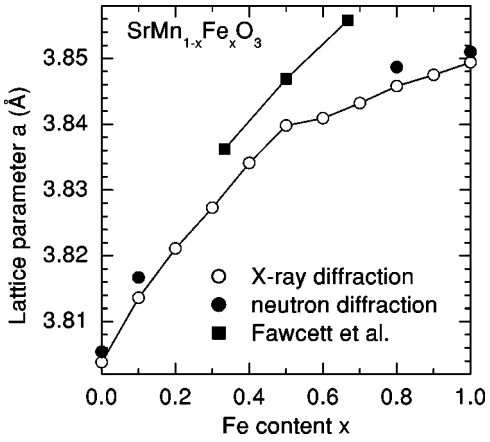

FIG. 2. Lattice parameter a for $SrMn_{1-x}Fe_xO_3$ samples (circles). Solid squares are plotted from Ref. 11 data.

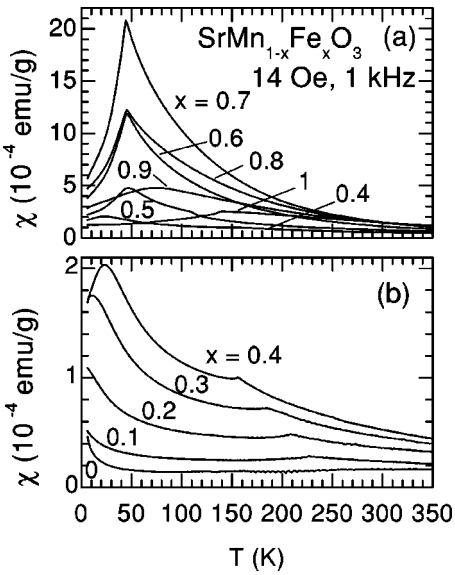

FIG. 3. ac susceptibility for $SrMn_{1-x}Fe_xO_3$ samples.

IV. MAGNETIC PROPERTIES

The ac susceptibility for $SrMn_{1-x}Fe_xO_3$ samples is presented in Fig. 3. For $x \leqslant 0.5$ and $x \geqslant 0.9$, we observe temperature dependencies that are characteristic of antiferromagnetic materials. For $0.3 \leqslant x \leqslant 0.8$ we also observed a cusp, which is a signature of spin-glass behavior. From these results we have determined Néel temperatures [defined as the temperatures for which $\chi(T)$ has a maximum slope] and the spin-glass freezing temperatures, T_f (defined as the temperatures where the susceptibility cusp reaches its maximum). We also observed additional magnetic properties that substantiate the presence of the spin-glass state in our samples. These properties will be discussed in detail throughout this section. Inverse susceptibility as a function of temperature is linear above T_N for $x<0.5$ and its intersection with the horizontal axis is negative, which points to antiferromagnetic interactions. $\chi^{-1}(T)$ for higher Fe contents $x=0.5-1$ is curved and its slope can be extrapolated either to a negative intersection when we analyze the temperature range just above T_N, or to a positive intersection when we take into account higher temperatures. This behavior has been observed in $SrFeO_3$ (Ref. 6) and is a result of the presence of both ferromagnetic and antiferromagnetic interactions in these materials.

The values of Néel temperature and the spin-glass freez-

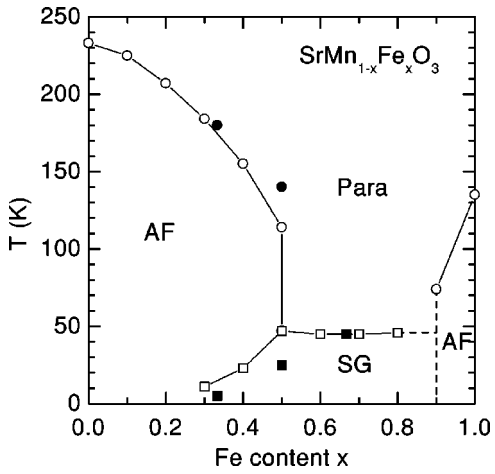

FIG. 4. Phase diagram for $SrMn_{1-x}Fe_xO_3$. Solid markers are data points from Ref. 11.

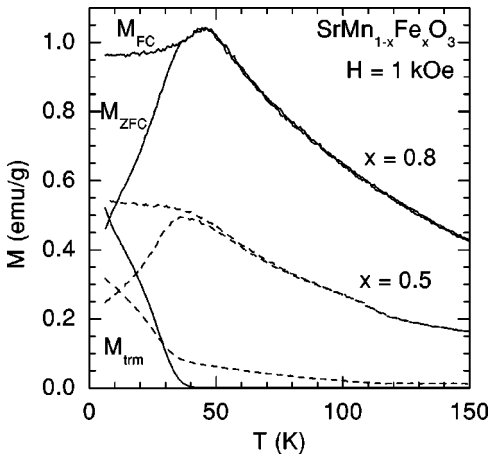

FIG. 5. Zero-field-cooled (M_{ZFC}), field-cooled (M_{FC}), and thermoremanent (M_{trm}) magnetizations for $SrMn_{0.5}Fe_{0.5}O_3$ (dashed lines) and $SrMn_{0.2}Fe_{0.8}O_3$ (solid lines) samples.

ing temperature are collected in the phase diagram in Fig. 4. Four distinct regions in the phase diagram are observed. For $x \leqslant 0.2$, only an antiferromagnetic phase is observed with T_N decreasing as x increases. A decrease of T_N has been explained for isoelectronic Ca and Ba lightly substituted in the cubic perovskite $SrMnO_3$,[4] a result of the *A*-site size variance $\sigma^2 = \Sigma y_i r_i^2 - (\Sigma y_i r_i)^2$, where r_i is the ionic size and y_i is the fractional occupancy of the *A* site.[5] This parameter describes the local variations of the Mn-O-Mn bond angle in the cubic region that exist even when the average Mn-O-Mn bond angle is equal to 180°. In the present case, the increase of the Fe content x increases the *B*-site size variance. This effect changes the local variation of the Mn-O-Mn bond angle even when the average structure is cubic and hence leads to lower T_N. Additionally, different magnetic *B*-site ions (Fe^{3+} or Fe^{5+}; see Sec. VI) randomly substituted for Mn^{4+} change the net exchange integral and introduce disorder, which also lowers T_N.

For $x = 0.3 - 0.5$, we observed both antiferromagnetic order and spin-glass behavior. Fawcett *et al.*'s results[11] are shown in Fig. 4 for comparison. Fawcett *et al.* also observed both antiferromagnetism and spin glass in the $x = 1/3$ and $x = 1/2$ samples. We have seen that for a given Fe content, when the oxygen content is increasing, T_N decreases and T_f increases. Therefore, the $x = 1/2$ oxygen-deficient sample shows higher T_N and lower T_f.

In the next region of the phase diagram, where $0.6 \leqslant x \leqslant 0.8$, only the spin-glass behavior can be observed. The spin-glass freezing temperature is almost constant in this region. This characteristic temperature is also nearly independent of the oxygen content. The magnitude of the ac susceptibility (see Fig. 3) is the largest for the $x = 0.7$ sample, which indicates the largest effective magnetic moment for this composition. The last region is close to $x = 1$, where only antiferromagnetic order can be observed.

The zero-field-cooled (M_{ZFC}) and field-cooled (M_{FC}) magnetizations, presented in Fig. 5 for $x = 0.5$ and $x = 0.8$, were measured in the magnetic field of 1 kOe. M_{ZFC} was measured on warming after cooling in a zero magnetic field and switching the magnetic field on at $T = 5$ K. M_{FC} was subsequently measured on cooling in the magnetic field. We can observe a difference between M_{ZFC} and M_{FC} below a certain temperature. This difference is typical for spin-glass systems. Thermoremanent magnetization (M_{trm}), which can be observed after field cooling to a temperature below T_f and switching off the magnetic field, is also a manifestation of the spin-glass behavior. The $x = 0.8$ sample shows this difference between M_{ZFC} and M_{FC} below a certain "irreversibility temperature" (T_{irr}).[16] $T_{irr} \sim 36$ K and is lower than T_f. M_{trm} decreases to zero at T_{irr} with increasing temperature. This sample shows a transition from the spin-glass state to the paramagnetic state. The $x = 0.5$ sample, which undergoes a transition from spin glass to the antiferromagnetic state, shows a significant difference between M_{ZFC} and M_{FC} above T_f. In addition, the thermoremanent magnetization can also be observed in the antiferromagnetic state above T_f up to T_N. This observation indicates substantial disorder in the antiferromagnetic state for the $x = 0.5$ sample. This phase is analogous to the "random antiferromagnetic state" observed in $Mn_{1-x}Fe_xTiO_3$.[17] Thermoremanent magnetization exhibits a slow decay in time, which is shown in the inset to Fig. 6(b).

We have fitted the formula[18]

$$M_{trm} = M_0 t^{-\beta} \tag{1}$$

to our experimental data and determined the parameters M_0 (the extrapolated to zero time magnetization) and the exponent β, which describe the dynamics of spin glasses. Equation (1) satisfactorily describes the time dependence of the thermoremanent magnetization in nearly the entire time window we span, except for short times $t < 500$ s where we can see some negative deviations from this time dependence. This formula, derived by Ogielski in Monte Carlo simulations, was used to describe the time decay of three-dimensional Ising spin glasses,[18] and also applied to $Mn_{0.5}Fe_{0.5}TiO_3$,[19] considered to be an "ideal" three-dimensional short-range Ising spin glass.[20] The temperature dependence of M_0 and β for $x = 0.5$ and $x = 0.8$ samples is presented in Fig. 6. M_0 systematically decreases with T for

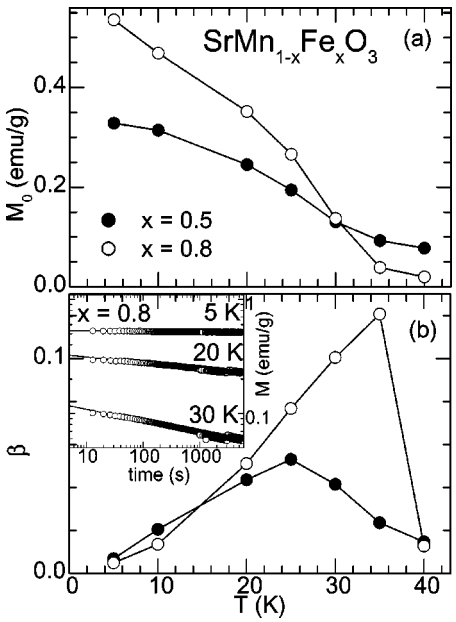

FIG. 6. Parameters of time decay of the thermoremanent magnetization for $SrMn_{0.2}Fe_{0.8}O_3$ (open circles) and $SrMn_{0.5}Fe_{0.5}O_3$ (solid circles). The lines are a guide to the eye. The parameters M_0 (a) and β (b) were determined from the fit using $M_{trm}=M_0 t^{-\beta}$. The inset to (b) shows the time dependence of M_{trm} for $SrMn_{0.2}Fe_{0.8}O_3$ and the fits of the above formula to the experimental data.

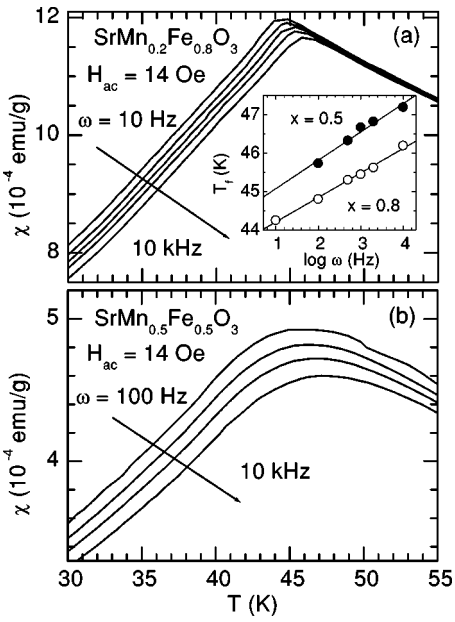

FIG. 7. Temperature dependence of ac susceptibility for $SrMn_{0.2}Fe_{0.8}O_3$ (a) and $SrMn_{0.5}Fe_{0.5}O_3$ (b) at several frequencies. Inset shows the linear dependence of T_f on log frequency.

both samples. It approaches zero at the irreversibility line for the $x=0.8$ sample. For the $x=0.5$ sample, M_0 remains substantially nonzero above T_f in the ''random antiferromagnetic state.'' The parameter β, which is a measure of the relaxation rate, for $x=0.8$, increases with T up to $T_{irr}=36$ K and rapidly drops above this temperature. The increase of $\beta(T)$ is not exponential as expected for an ''ideal'' spin glass.[19] The $\beta(T)$ dependence is different for the $x=0.5$ sample, which shows a maximum at $T\sim 0.5T_f$ and a subsequent decrease. This behavior may be a result of the presence of antiferromagnetic order in the spin-glass state, which inhibits the decay rate of the thermoremanent magnetization.

In Fig. 7, we present the ac susceptibility for $SrMn_{0.2}Fe_{0.8}O_3$ and $SrMn_{0.5}Fe_{0.5}O_3$ samples measured at several frequencies in an ac magnetic field of constant amplitude $H_{ac}=14$ Oe. One can observe a decrease of the ac susceptibility below T_f with increasing frequency, and a shift of T_f towards higher temperatures. This confirms that the observed cusp in the ac susceptibility is related to spin-glass behavior.[20] For the $x=0.8$ sample, the ac susceptibility is independent of frequency above T_f (in the paramagnetic state). For the $x=0.5$ sample, a significant frequency dependence of χ can still be observed, which again points to a frustration of the antiferromagnetic state above the spin-glass freezing temperature. The inset to Fig. 7(a) shows the dependence of T_f on log frequency. The linear fit to $T_f(\log\omega)$ gives relative temperature shift vs frequency $\Delta T_f/[T_f\Delta(\log\omega)]=0.0147\pm0.008$ and 0.0167 ± 0.017 for $x=0.8$ and $x=0.5$, respectively. These values are similar to those observed for canonical spin glasses such as $PdMn$ and $NiMn$.[20]

V. RESISTIVITY

The temperature dependence of resistivity for $SrMn_{1-x}Fe_xO_3$ samples is presented in Fig. 8. The resistivity is relatively low ($\sim 1\ \Omega$ cm at room temperature) for $SrMnO_3$ and increases by over four orders of magnitude on substitution of 10% Fe for Mn. It reaches a maximum for $x=0.1$ and decreases with further Fe substitution. $\rho(T)$ shows mostly semiconducting dependence. We were able to fully

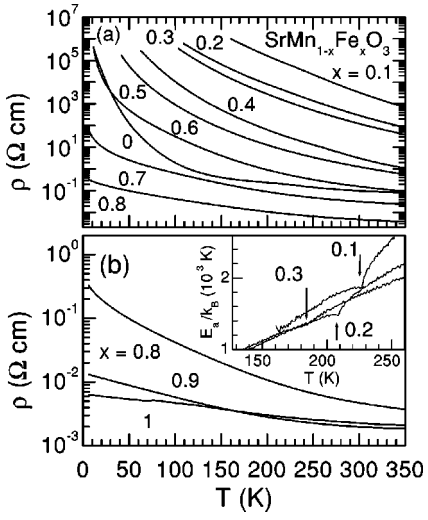

FIG. 8. Temperature dependence of resistivity for $SrMn_{1-x}Fe_xO_3$ samples. The inset shows the calculated derivative $E_a/k_B=d\ln(\rho)/d(1/T)$ for $x=0.1-0.3$.

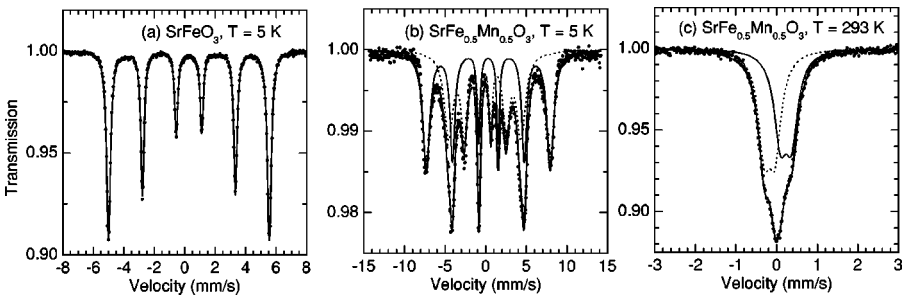

FIG. 9. Mössbauer spectra for $SrFeO_3$ and $SrMn_{0.5}Fe_{0.5}O_3$ samples. The fit of the two-site model for $SrMn_{0.5}Fe_{0.5}O_3$ is represented by thin solid lines for Fe^{3+} and dotted lines for Fe^{5+}.

oxygenate $SrFeO_3$ only in the powder form under high pressure. This powder was used for magnetic, structural, and Mössbauer measurements, but could not be used for resistivity measurements. Polycrystalline pellets were synthesized, but were slightly oxygen deficient. Therefore, these pellets of $SrFeO_{3-\delta}$ show a small increase of resistivity on decreasing temperature as seen in Fig. 8. Assuming thermally activated resistivity, $\rho=\rho_0\exp(E_a/k_BT)$, we estimated the activation energy for $SrMn_{1-x}Fe_xO_3$. The inset to Fig. 8(b) shows the calculated derivative $E_a/k_B=d\ln(\rho)/d(1/T)$ for $x=0.1-0.3$. We have found that calculated in this way E_a/k_B is temperature dependent (not constant with respect to temperature as expected for the simple thermal activation conduction model). The negative kinks, which are marked with arrows, denote T_N. We also checked other models of conduction by introducing a temperature-dependent prefactor to the formula $\rho\propto T^s\exp[(T_0/T)^p]$.[21] The best description of our data can be obtained with $s=8-9$ for this formula. The physical meaning of this value is not yet clear because this value is much higher than that proposed in the framework of the existing models (e.g., $s=1/2$ in Mott's variable range hopping model[22] or $s=1$ in the small polaron model[23]).

VI. MÖSSBAUER SPECTROSCOPY

Stoichiometric $SrMn_{1-x}Fe_xO_3$ samples were examined by applying Mössbauer spectroscopy on the ^{57}Fe isotope that is 2% abundant in the material. Through a careful analysis of the magnetic hyperfine field and the isomer shift, Mössbauer spectroscopy provides a way of ascertaining whether iron is in different chemical or crystallographical environments, as well as its valence state. High-spin Fe^{3+}, Fe^{4+}, and Fe^{6+} have room-temperature isomer shifts in the range 0.1 to 0.6, -0.2 to 0.2, and -0.8 to -0.9 mm/s, respectively (relative to α-Fe).[24] There are fewer studies of the isomer shift for Fe^{5+}; therefore it is less well understood. The magnetic hyperfine field is dominated by the Fermi contact interaction which gives rise to about 550 kOe for high-spin Fe^{3+} having a mean spin of 5/2 for the $3d$ electrons. Thus, a general rule is that $\sim$110 kOe corresponds to $\sim$1 Bohr magneton (one unpaired electron). These rules can substantially change due to covalency effects. Increasing the covalency between iron and oxygen tends to produce lower isomer shifts, and reduce the effective number of unpaired electrons which leads to lower magnetic hyperfine fields. In a metallic material polarized conduction electrons also affect the magnitude of the hyperfine field.

The parent compound, $SrFeO_3$, is known to be a metallic conductor that orders into a helical antiferromagnetic structure at low temperatures due to the competition between ferromagnetic nearest neighbors and antiferromagnetic next-nearest neighbors.[6] As seen in Fig. 9, $SrFeO_3$ exhibits a set of sharp magnetically split lines (0.24-mm/s linewidth) at 5 K. In the paramagnetic state at 293 K, the spectrum consists only of a slightly broadened single line (0.27-mm/s linewidth). Thus, Fe exists in only one valence state from 5 K to room temperature. Charge balance suggests that $SrFeO_3$ forms with iron in the $+4$ valence state. This is confirmed by the measured isomer shift of 0.059 mm/s at 293 K (0.154 mm/s at 5 K). The low magnetic field of 327 kOe would also indicate that this material has a magnetic moment of $3\mu_B$ rather than the expected $4\mu_B$, but the low magnetic field may be due to the nearly delocalized character of the electron in the e_g orbital of Fe^{4+} with comcomitant lowering of the net field by the polarized conduction electrons. The quadrupole splitting for this material is nearly zero (~ -0.019 mm/sec) at 293 K, agreeing with the values reported in the literature.[25] This result indicates the absence of any extensive static Jahn-Teller distorted FeO_6 octahedra even though high-spin Fe^{4+} is a likely candidate for a Jahn-Teller ion due to the single electron in the e_g orbital.[12] However, a dynamic Jahn-Teller effect is not ruled out. Due to the lifetime of the excited nuclear state, the ^{57}Fe nucleus is sensitive to fluctuating environments that fluctuate on a time scale longer than 10^{-11} sec. A fast dynamic Jahn-Teller effect where the electronic hopping is enhanced by the delocalized character of the e_g electron could result in electric quadrupole fluctuation times that are too short for the Fe nuclei to detect. Thus, the electric quadrupole interaction effectively averages to near zero. Thus, the high-pressure synthesis technique appears to be successful in producing highly stoichiometric compounds of metallic $SrFeO_3$ and is a sound technique to produce stoichiometric samples of $SrMn_{1-x}Fe_xO_3$.

Measurements were made on $SrMn_{1-x}Fe_xO_3$ at various temperatures to characterize the charge disproportionation properties of iron in the spin-glass, antiferromagnetic, and paramagnetic phases. Charge disproportionation has been observed in the highly nonstoichiometric form of $SrMn_{1-x}Fe_xO_{3-\delta}$ as well as in $CaFeO_3$.[11,26] Charge balance would dictate that the valence state of Fe should be $+4$ (since Fe and Mn share the same crystallographic sites for the first material and Mn exists in only the $+4$ valence state[11]). What is usually observed is a two-site iron Mössbauer spectrum indicating that Fe exists in two valence states rather than in a single, pure valence state of $+4$. The existence of two different Fe valence states provides evidence for

TABLE I. Hyperfine parameters deduced from Mössbauer spectra. H_{eff} is the mean magnetic hyperfine field; ε is the effective quadrupole splitting; δ_{is} is the isomer shift relative to α-Fe; Γ_3 and Γ_1 are the linewidths of the inner and outer lines, respectively, in the spectra (at 293 K, there is only a single line), and Area is the relative area under each subspectra. The areas for the two charge states of Fe in $SrMn_{0.5}Fe_{0.5}O_3$ are equal within statistical error.

Compound	T (K)	H_{eff} (kOe)	ε (mm/s)	δ_{is} (mm/s)	Γ_3/Γ_1 (mm/s)	Area (%)
$SrMn_{0.5}Fe_{0.5}O_3$	5	480(1)	−0.009(9)	0.435(5)	0.4/0.99	52
		279(1)	−0.04(2)	0.03(1)	0.52/1.5	48
	293		0.289(4)	0.350(3)	0.39	48
			0.265(3)	−0.059(3)	0.36	52
$SrFeO_3$	5	327(1)	−0.001(1)	0.154(1)	0.24	100
	293		−0.02(4)	0.059(1)	0.27	100

a charge disproportionation as follows: $2\,Fe^{4+} \rightleftarrows Fe^{(4-\delta)+} + Fe^{(4+\delta)+}$, where δ varies from 0 to 1 depending on the covalency between iron and oxygen.

We have observed the presence of charge disproportionation in highly stoichiometric forms of $SrMn_{1-x}Fe_xO_3$. Thus, oxygen vacancies are not a factor in the charge disproportionation properties.[11] As Mn was added to $SrFeO_3$, the spectra revealed the presence of two distinct Fe sites having different magnetic hyperfine fields and isomer shifts. The spectra for one of the samples, $SrMn_{0.5}Fe_{0.5}O_3$, are shown in Fig. 9 and the sample data is given in Table I. In this table, ε is the effective quadrupole splitting, which is defined as $\varepsilon = eQV_{zz}(3\times\cos^2\theta - 1)/4$ in a magnetically ordered state and $\varepsilon = eQV_{zz}/2$ in a paramagnetic state, where eQ is the nuclear quadrupole moment, V_{zz} is the z component of the electric-field gradient tensor, and θ is the angle between the V_{zz} axis and H_{eff}. From this data the Fe ions appear to exist, in nearly equal proportions, in two valence states in the paramagnetic, antiferromagnetic, and spin-glass phases (by examining the area under each Mössbauer subspectra). Mn is known to exist in a valence state close to +4 through x-ray-absorption spectroscopy chemical shift measurements on nonstoichiometric compounds.[11] Since Mn does not charge disproportionate, then, because the Fe sites occur in nearly equal proportions, the Fe site having the largest magnetic field (480 kOe at 5 K) was assigned a +3 valence state, and a +5 valence state was assigned to the other Fe site. The Fe site assigned a +3 valence state also has an isomer shift (0.35 mm/sec at 293 K) that lies near that expected for Fe^{3+} (between 0.1 and 0.6 mm/s for a high-spin state). This is exactly what one would expect for fully oxygenated $SrMn_{0.5}Fe_{0.5}O_3$—that the average valence state of Fe would be +4.

The actual environment around each Fe atom is rather complicated. Fe^{3+}, Fe^{5+}, and Mn^{4+} can all occupy the same site in this cubic perovskite. Thus, since each ion has a different ionic size, there must be a disordered array of Fe^{3+}, Fe^{5+}, and Mn^{4+} oxygen octahedra of differing sizes and distortions throughout the lattice. It is worth noting that for fully oxygenated samples the quadrupole splitting at room temperature is smaller than that for nonstoichiometric ones.[11] This reflects a less distorted local environment, without oxygen vacancies, for the stoichiometric compositions. The distribution of different ions over the crystallographic lattice gives rise to the slight broadening of the Mössbauer lines in the paramagnetic region. In addition, there are competing ferromagnetic and antiferromagnetic interactions in both the spin-glass region and the antiferromagnetic region (since the parent compound, $SrFeO_3$, has a helical antiferromagnetic structure). The much broader Mössbauer lines observed in the magnetically ordered regions for both the antiferromagnetic and spin-glass phases (the outer linewidths were all greater than 1 mm/sec over the whole temperature region in Fig. 10) are likely due to competing magnetic interactions between the transition-metal cations, Fe^{+3}, Fe^{+5}, and Mn^{+4}. Since the materials under study have a random distribution of Fe^{+3}, Fe^{+5}, and Mn^{+4} ions throughout the lattice, different sizes and magnetic moments of these ions lead to a variation in the structural and magnetic environments around the Fe sites, resulting in the distribution of hyperfine parameters observed in the Mossbauer spectra. Thus, as a function of temperature and composition, from $0.1 \leqslant x \leqslant 0.9$, there is a pronounced broadening of the Mössbauer linewidths in both the antiferromagnetic and spin-glass phases. Fitting the spectra with a distribution of magnetic hyperfine fields, quadrupole splittings, and isomer shifts did

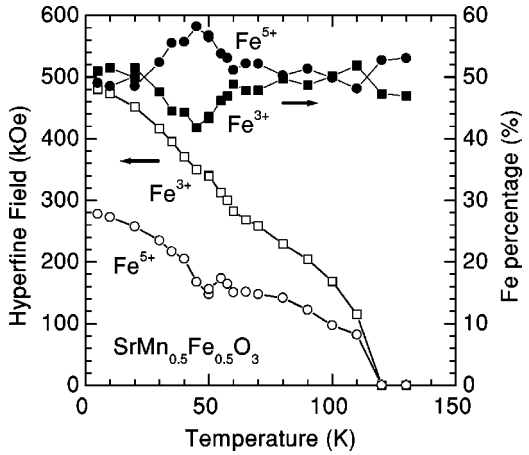

FIG. 10. Hyperfine fields (open markers) and the percentage of Fe^{3+} and Fe^{5+} (solid markers) determined from Mössbauer spectra for $SrMn_{0.5}Fe_{0.5}O_3$. The spectra were fitted using a two-site Lorentzian model.

not reveal any clearly distinguishable characteristics between the antiferromagnetic and spin-glass phases—there was a significant amount of frustration in both phases arising from the competing magnetic interactions that also occur in both phases. However, since the spectra revealed two easily distinguishable sites, the fits to the spectra were made using a simple Lorentzian model which gives average hyperfine field values. The variation of the average magnetic hyperfine field with temperature for $SrMn_{0.5}Fe_{0.5}O_3$ is given in Fig. 10. Due to the complicated nature of the magnetic interactions, the magnetization curves do not follow the typical $S=5/2$ or $S=3/2$ Brillouin curves. The equal proportion of Fe^{3+} to Fe^{5+} is nearly maintained over all temperatures. However, near the spin-glass/antiferromagnetic transition temperature, there is a deviation from this behavior indicating the presence of more complex behavior. Three-site models have been applied to other materials where Fe charge disproportionates into $+3$ and $+5$ valence states, such as in $La_{1-x}Sr_xFeO_3$.[14] However, applying such a model does not eliminate the anomaly near the spin-glass transition temperature. Further investigations are under way to understand the existence of this valence state anomaly near the spin-glass/antiferromagnetic phase boundary.

VII. SUMMARY

In summary, we have studied the cubic perovskite $SrMn_{1-x}Fe_xO_3$ ($0 \leqslant x \leqslant 1$) system. By ac susceptibility studies of fully oxygenated samples, we have constructed the magnetic phase diagram. We have found antiferromagnetic ordering for the lightly and heavily substituted material, while intermediate substitution leads to spin-glass behavior. Close to the $SrMn_{0.5}Fe_{0.5}O_3$ composition these two types of ordering coexist and affect one another. By Mössbauer investigations, we have observed the presence of charge disproportionation of iron to nearly equal proportion of Fe^{3+} to Fe^{5+} in stoichiometric $SrMn_{0.5}Fe_{0.5}O_3$ and the single-valence state of Fe^{4+} in $SrFeO_3$. The increase of Fe content, x, is accompanied by stronger covalency of the Fe-O bond, which leads to the shortening of this bond, a decrease of resistivity, lower isomer shifts, and magnetic hyperfine fields.

ACKNOWLEDGMENTS

This work was supported by the DARPA/ONR, NSF-DMR-0105398, and the State of Illinois under HECA. IPNS at Argonne National Laboratory is supported by the U.S. Department of Energy, BES-MS, under Contract No. W-31-109-ENG-38.

*Also at Institute of Nuclear Physics, ul. Radzikowskiego 152, Kraków, Poland.

[1] Y. Tokura and N. Nagaosa, Science **288**, 462 (2000).
[2] S. Hebert, A. Maignan, C. Martin, and B. Raveau, Solid State Commun. **121**, 229 (2002), and references therein.
[3] T. Negas and R. S. Roth, J. Solid State Chem. **1**, 409 (1970).
[4] O. Chmaissem, B. Dabrowski, S. Kolesnik, J. Mais, D. E. Brown, R. Kruk, P. Prior, B. Pyles, and J. D. Jorgensen, Phys. Rev. B **64**, 134412 (2001).
[5] L. M. Rodriguez-Martinez and J. P. Attfield, Phys. Rev. B **54**, R15622 (1996); **58**, 2426 (1998).
[6] T. Takeda, Y. Yamaguchi, and H. Watanabe, J. Phys. Soc. Jpn. **33**, 967 (1972).
[7] J. B. MacChesney, R. C. Sherwood, and J. F. Potter, J. Chem. Phys. **43**, 1907 (1965).
[8] H. Yamada, M. Kawasaki, and Y. Tokura, Appl. Phys. Lett. **80**, 622 (2002).
[9] J. P. Hodges, S. Short, J. D. Jorgensen, X. Xiong, B. Dabrowski, S. M. Mini, and C. W. Kimball, J. Solid State Chem. **151**, 190 (2000).
[10] M. Abbate, G. Zampieri, J. Okamoto, A. Fujimori, S. Kawasaki, and M. Takano, Phys. Rev. B **65**, 165120 (2002), and references therein.
[11] I. D. Fawcett, G. M. Veith, M. Greenblatt, M. Croft, and I. Nowik, Solid State Sci. **2**, 821 (2000).
[12] M. Takano, N. Nakanishi, Y. Takeda, S. Naka, and T. Takeda, Mater. Res. Bull. **12**, 923 (1977).
[13] M. Takano and Y. Takeda, Bull. Inst. Chem. Res., Kyoto Univ. **61**, 406 (1983).
[14] S. E. Dann, D. B. Currie, M. T. Weller, M. F. Thomas, and A. D. Al-Rawwas, J. Solid State Chem. **109**, 134 (1994).
[15] D. G. Hinks, B. Dabrowski, J. D. Jorgensen, A. W. Mitchell, D. R. Richards, and D.-L. Shi, Nature (London) **333**, 836 (1988); B. Dabrowski, O. Chmaissem, J. Mais, S. Kolesnik, J. D. Jorgensen, and S. Short, J. Solid State Chem. **170**, 154 (2003).
[16] A. M. O. De Almeida and D. J. Thouless, J. Phys. A **11**, 983 (1978).
[17] A. Ito, H. Aruga, M. Kikuchi, Y. Syono, and H. Takei, Solid State Commun. **66**, 475 (1988).
[18] A. T. Ogielski, Phys. Rev. B **32**, 7384 (1985).
[19] A. Ito, H. Aruga, E. Torikai, M. Kikuchi, Y. Syono, and H. Takei, Phys. Rev. Lett. **57**, 483 (1986).
[20] J. A. Mydosh, *Spin Glasses: an Experimental Introduction* (Taylor & Francis, London, 1993), and references therein.
[21] W. N. Shafarman, D. W. Koon, and T. G. Castner, Phys. Rev. B **40**, 1216 (1989).
[22] N. F. Mott, J. Non-Cryst. Solids **1**, 1 (1969).
[23] D. C. Worledge, L. Miéville, and T. H. Geballe, Phys. Rev. B **57**, 15 267 (1998).
[24] N. N. Greenwood and T. C. Gibb, *Mössbauer Spectroscopy* (Chapman and Hall, London, 1971), p. 91.
[25] P. K. Gallagher, J. B. MacChesney, and D. N. E. Buchanan, J. Chem. Phys. **41**, 2429 (1964).
[26] Y. Takeda, S. Naka, M. Takano, T. Shinjo, T. Takeda, and M. Shimada, Mater. Res. Bull. **13**, 61 (1978).